# Forward-collected simultaneous fluorescence lifetime imaging and coherent anti-Stokes Raman scattering microscopy

**Aaron D. Slepkov,[a] Andrew Ridsdale,[a] Huei-Ning Wan,[b] Ming-Hao Wang,[b] Adrian F. Pegoraro,[a,c] Douglas J. Moffatt,[a] John P. Pezacki,[a] Fu-Jen Kao,[b] and Albert Stolow[a,c]**
[a]National Research Council of Canada, Steacie Institute for Molecular Sciences, Ottawa, Ontario, K1A 0R6 Canada
[b]National Yang-Ming University, Institute of Biophotonics, 155, Li-Nong Street, Section 2, Taipei 11221, Taiwan
[c]Queen's University, Department of Physics, 99 University Avenue, Kingston, Ontario K7L 3N6 Canada

**Abstract.** We demonstrate the simultaneous collection and separation of femtosecond-laser-based forward-collected coherent anti-Stokes Raman scattering (F-CARS) and two-photon-excitation-induced fluorescence lifetime images (FLIM) using time-correlated single photon counting (TCSPC). We achieve this in a nondescanned geometry using a single multimode fiber without significant loss of light, field of view, and most importantly, TCSPC timing fidelity. In addition to showing the ability to separate CARS images from FLIM images using time gating, we also demonstrate composite multimodal epicollected FLIM imaging with fiber-collected F-CARS imaging in live cells.  [DOI: 10.1117/1.3490641]

Keywords: scanning microscopy; fiber optic applications; nonlinear optics; Raman spectroscopy; laser-induced fluorescence.

Paper 10168SSR received Mar. 29, 2010; revised manuscript received May 28, 2010; accepted for publication Jun. 2, 2010; published online Feb. 1, 2011.

## 1 Introduction

Time-correlated single photon counting (TCSPC)-based fluorescence lifetime imaging microscopy (FLIM) is a powerful tool for studying structure and dynamics in live cells and tissues.[1,2] In particular, within the framework of Förster resonance energy transfer (FRET),[1,3] FLIM is used to resolve molecular interactions on the sub-10-nm length scale. There is a natural desire to integrate FRET or FLIM with the sub-diffraction-limited spatial resolution and sectioning capabilities of nonlinear optical microscopy modalities such as two-photon excitation fluorescence (TPEF), second-harmonic generation (SHG), and coherent anti-Stokes Raman scattering (CARS). Thus far, FRET has been combined with TPEF[1,3] and SHG,[4] but not with CARS. Compared with other nonlinear optical imaging methods, CARS microscopy offers a unique *label-free* modality that images cells and tissues based on their natural chemical composition. CARS microscopy is particularly suited to (and most often used for) imaging of lipid-rich tissue and cellular structures.[5] The combination of CARS and FRET would provide complimentary imaging modalities for probing molecular interactions in the vicinity of lipid-rich cellular architecture. A specific example would include studying the role of and interaction between intracellular lipid droplets and fluorescently tagged hepatitis-C virus (HCV) core protein by performing colocalization experiments, thereby elucidating the HCV infectious pathways. However, unlike TPEF, which is emitted isotropically, the coherent and phase-matched nature of the CARS process leads to a predominance of anti-Stokes emission in the forward direction.[6] Strictly speaking, no backward-directed CARS is expected in bulk homogeneous media. It has been found, however, that under tight focusing conditions, both subwavelength particles and interfaces emit epidirected CARS (E-CARS) signals.[7] Forward-collected CARS (F-CARS) from larger structures typically yields a signal two orders of magnitude greater than E-CARS.[6] It is worth noting that in highly scattering tissue, the presence of some backscattered F-CARS means that the backward-collected CARS signal often represents a mix of E- and F-CARS, which complicates subsequent image interpretation.[8]

Establishing a FLIM-CARS microscope represents an important step toward conjoining FRET and CARS capabilities. Recently, Huser et al. demonstrated the incorporation of CARS with TCSPC and FLIM.[8,9] Because CARS is a nearly instantaneous process (on the order of the laser pulse duration), it is indistinguishable from the instrument response function (IRF) of the TCSPC apparatus and can thus be separated from the nanosecond-timescale fluorescence decay by time-gated analysis. However, efforts to combine FLIM with CARS have been hampered by configurations where signals are collected in the descanned backward direction. This is at odds with the maximal CARS signal being in the forward direction. One solution is to reflect the F-CARS back through the sample, collecting the signal via epidetection.[8–10] A second option is to use detectors in the forward direction without descanning. This can work well with large-area photomultiplier tubes (PMTs), but is problematic when using sensitive, ultrafast, photon-counting detectors such as single-photon avalanche photodiodes (SAPDs) because of their small active area. Furthermore, this geometry adds considerable complexity to the microscope and requires nontrivial light shielding to enable high contrast detection.

A solution to this problem is to relay the forward-collected signal to off-board detectors with an optical fiber. The

Address all correspondence to: Aaron Slepkov, National Research Council of Canada, Steacie Institute for Molecular Science, Rm. 2077,100 Sussex Drive, Ottawa, Ontario, K1A 0R6, Canada. Tel: 613-990-0143; E-mail: slepkov@gmail.com

1083-3668/2011/16(2)/021103/7/$25.00 © 2011 SPIE

advantages of fiber-coupling the forward-propagating signals are immediately evident: the small fiber core and strict coupling conditions inherently simplify light rejection of both scattered laser and ambient light; bulky detectors and their electronics can be kept away from the microscope, allowing easier sample preparation; and the fiber-coupled signals can be easily relayed to any number of detectors and spectrometers, greatly increasing the modality options of a fixed microscope setup. There have been real and perceived obstacles to this approach. First, coupling of the laser scanning signal to a submillimeter fiber core without untenable loss of light and image distortion is nontrivial. More important to TCSPC, however, is the need to relay photons with high timing fidelity. We feel that it is this last challenge that has largely prevented this approach from being widely adopted.[11,12] A recent compromise has been the use of large fiber bundles for this purpose.[12–14] This approach maintains some of the aforementioned advantages of fiber coupling, but the large bundle face can allow for the relaying of significant scattered light, and bundles further suffer loss of light from the inherent light rejection in the interstitial regions of the fiber packing. Finally, the bundle suffers from a significant amount of temporal broadening and skewing of photon arrival times as a function of coupling angle [numerical aperture (NA)].[12,13]

In this paper we describe the simple modification of a commercial inverted microscope for collection of transmitted nondescanned light through a multimode optical fiber. We show that over 50% coupling and field of view (FOV) can be obtained, with minimal image distortion. Finally, we demonstrate that meters-long fiber can be used to relay TCSPC data with excellent timing fidelity, allowing for single- or multiple-detector FLIM + CARS imaging.

## 2 Experiments

### 2.1 *Two-Photon Excitation Fluorescence and CARS Microscopy*

A Ti:sapphire oscillator (Coherent Mira900) produces 60-fs pulses with a 80-MHz repetition rate, at a wavelength adjustable between 750 to 1000 nm. An 805-nm output was used in the experiments presented here. A variable beamsplitter (a half-wave plate followed by a polarizing beam cube) sends 200 to 250 mW to a commercial photonic crystal fiber (PCF) module (NKT Photonics, FemtoWhite CARS) for the creation of Stokes light to be used for CARS imaging, and the remainder (>1 W) comprises the pump beam used for TPEF, CARS, and SHG imaging modalities. A set of long-pass filters spectrally selects ($\lambda > 950$ nm) the Stokes supercontinuum before it is sent to matched SF-10 glass prisms for dispersion engineering, en route to a dichroic beam combiner (Chroma Technology cdxr950). The pump beam is likewise passed through a separate prism pair for dispersion engineering, before being sent to a computer-controlled delay stage and then recombined with the Stokes beam at the combiner. The combined beams are then routed to the microscope. An Olympus 40X 1.15 NA UAPO water immersion lens with a cover slip correction collar is used as the objective. A 400- to 700-nm bandpass filter (E700sp, Chroma Technology) is used to discriminate TPEF, SHG, sum frequency generation (SFG), and anti-Stokes signals from the pump and Stokes beams. As we have previously reported,[15,16] our single-femtosecond-laser-source CARS microscope relies on chirp-matching of the pump and Stokes pulses for optimal CARS signal and spectral resolution. Furthermore, the probed Raman frequency can be rapidly scanned by continuous adjustment of the time overlap of the two pulses using a computer-controlled delay stage on the pump arm. For imaging lipids at $\sim$2880 $cm^{-1}$ (aliphatic C-H stretch) we temporally overlap the 805-nm pump pulse with the 1050-nm component of the broadband Stokes spectrum at the focus of the objective, generating an anti-Stokes pulse at 650 nm. The CARS signal varies linearly with the instantaneous Stokes power and quadratically with the pump power. Concurrent with the two-beam CARS response, the TPEF signal is emitted isotropically, and is quadratically proportional to the pump power. The Stokes power is typically insufficient to significantly contribute to either degenerate (Stokes-Stokes) or nondegenerate (Stokes-pump) two-photon excitation in biological samples. For CARS imaging, we input 3 to 10 mW of total (>950 nm) Stokes power and 30 to 200 mW of pump power into the laser-scanning unit and microscope. The amount of pump power used depends on the application and the brightness of the image; 100 mW is typical for live-cell imaging.

### 2.2 *Microscope Geometry*

An Olympus Fluoview 300 inverted laser-scanning microscope that is typically set up for descanned epidetection had the collection optics modified in both the forward direction and epidirection. The fluorescence dichroic separator in the descanned epidirection (after the confocal pinhole and within the FV300 scanning unit) was reengineered so that the descanned signal could be coupled to either the built-in large area PMTs or to the external detectors for TCSPC (Hamamatsu H5783-02). Time-resolved detection is achieved with the repetition rate of the Ti:sapphire laser serving as the time base. The scanning synchronization signal of the FV300 is used to coordinate timing of the TCSPC-based FLIM module (PicoHarp 300, Picoquant GmbH).

The forward-propagating signal pathway has been modified to enable collection through a multimode fiber. The signal is collected by a long-working-distance, 0.55-NA condenser. Using a 45-deg mirror, the signal is then directed through dichroic filters to a high-NA aspheric lens (Thorlabs, C330TME-A), which collects the signal into a standard multimode fiber (Thorlabs FT600EMT, 600-$\mu$m core, 0.39 NA). The fiber can be used to direct the signal to any desired detector, but for CARS microscopy a red-sensitivity-enhanced PMT (Hamamatsu R3896) is typically used. A photo of this adapter and a schematic of the coupling optics train are provided in Fig. 1. Under typical operation, we collect the CARS signal in the forward direction while forward-propagating SHG and TPEF signals (as well as both Stokes and pump pulses) are blocked by bandpass filters.

### 2.3 *Sample Preparation*

In this article we show images of African violet pollen, octadecene oil drops in fluorescein-dyed water, and live human hepatoma cell line (HuH-7). Unstained pollen samples were dry-extracted from flower stamens and suspended in water. For a sample of oil droplets in a fluorescing background, we continually diluted samples of fluorescein in water until TPEF signals in the forward direction were roughly matched in intensity to

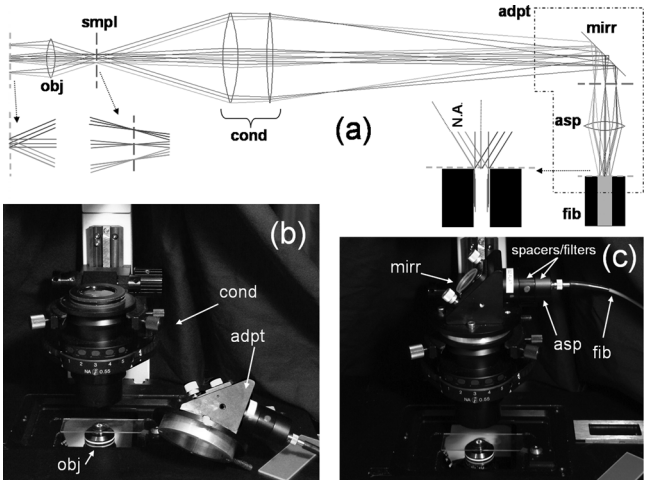


**Fig. 1** (a) Fiber-coupling geometry (not to scale): obj: objective; smpl: sample plane; cond: condenser; adpt: fiber coupling adapter; mirr: mirror; asp: aspheric lens; and fib: multimode fiber. Cyan dashed line and magenta dashed line denote objective back aperture conjugate planes and sample conjugate planes, respectively. (b) and (c) Annotated photos of microscope with fiber-coupling adapter beside and affixed to the condenser housing, respectively. (Color online only.)

CARS signals from octadecene. We then dispersed a droplet of octadecene into the solution, forming droplets a few microns in diameter, and set this on a microscope slide and cover slip. Fine tuning of the relative CARS and TPEF signals was obtained by minor adjustment of Stokes power. HuH-7 cells were grown in Dulbecco's modified Eagle's medium (DMEM) supplemented with 100 nM nonessential amino acids, 50 U/ml penicillin, 50 $\mu$g/ml streptomycin, and 10% (v/v) fetal bovine serum, as detailed elsewhere.[17]

## 3 Results and Discussion

### 3.1 *The Optics of Fiber Coupling Nondescanned Light*

The key to coupling the nondescanned light into the fiber in the forward direction with minimal field-of-view aperturing or distortion is to reimage the back aperture conjugate plane of the objective. To enable coupling, this collimated beam must have a spot size smaller than the fiber core. Depending on the initial position in the sample, the incoming beam will impinge on the fiber at an angle, and for efficient coupling this must be contained within the NA of the fiber [see Fig. 1(a)]. The optimal coupling geometry represents an optimization of the fiber core diameter, the numerical aperture of the fiber, the condenser magnification, and the working aperture size of the aspheric fiber-coupling lens. Figure 1(a) outlines the optical train from the objective to the fiber: the scan lens and 40X objective project the (22-mm maximum) scan field onto the sample. This (550-$\mu$m maximum) scanned image area is transferred by the condenser to a 2.5-mm-sized image plane. A 3.1-mm-focal-length 0.68-NA aspheric lens collimates this light, converting the radial (or lateral) position in the image to the output angle of collimated light. Thus, 3.1 mm away from this aspheric lens we image the back focal plane of the objective—the light is now an ~550-$\mu$m-diameter collimated beam—onto the 600-$\mu$m-diameter fiber core. The edge of the 2.5-mm image area (1.25 mm radially removed from the optical axis) corresponds to an incoming angle of 21.9 deg, representing a NA of 0.37, which is within the 0.39 NA of the multimode fiber. Thus, we have chosen this particular aspheric lens as a good match for fiber coupling our microscope images into this specific fiber. With ideal alignment and optical placement we thus expect little loss in field of view over the entire scan range. In practice, slight imperfections in the placement of the fiber and the coupling asphere, as well as in microscope alignment, can lead to significant loss in the FOV. One particular culprit for loss of FOV is the placement of the fiber face away from the objective back aperture conjugate plane: the fiber face seems to be at an "infinity space" because all the beams are collimated. However, because the beams are angled into the fiber (coming together at the face), one would get some loss in the beams from the periphery of the FOV if the fiber is not exactly located at the appropriate conjugate plane. For example, we estimate that if the asphere is misaligned by 1 mm (axially), there will be noticeable loss of light from the edges of the FOV (but not from on-axis). It is important to reiterate that we are not imaging the sample plane onto the fiber face, as one would onto a camera. Thus, at the position of the fiber face, the signal looks like a stationary spot with a changing incoming angle, rather than a smaller, raster-scanning spot as it appears away from this plane.

Figure 2 presents a comparison of different possible collection geometries. In the forward direction, either a fiber was used

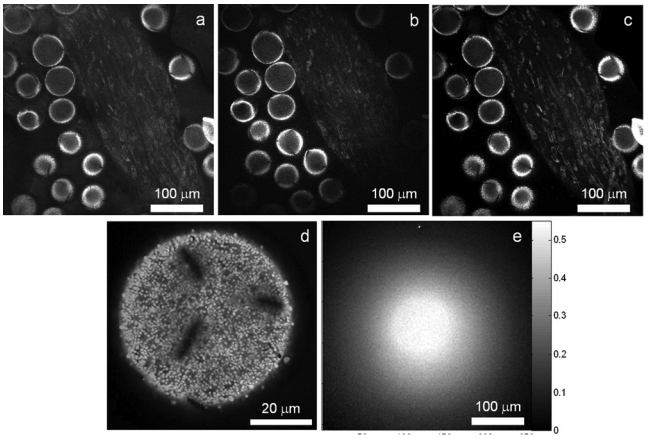


**Fig. 2** TPEF images of African violet pollen in water. (a) Forward-collected nondescanned detection with a PMT placed directly at a conjugate plane of the objective back aperture. All room lights are turned off and the microscope is covered by a black shroud. (b) Forward-collected nondescanned detection through a multimode fiber placed at the same location, directly illustrating the effect of loss of FOV. The microscope is uncovered, and considerable ambient room light is present. Slight changes in field of view (FOV) compared to (a) are due to a small drift in focal plane. (c) Concurrent descanned epidetected confocal imaging onto built-in detectors, for comparison. Ambient lighting conditions are the same as in (b); FOV is identical to (a). (d) Overlaid images of concurrently collected epidetected TPEF (green) and fiber-collected CARS at 2880 $cm^{-1}$ (red) showing the quality of image obtained near the center of the microscope FOV. (e) A measure of coupling efficiency and FOV aperturing, obtained by comparing TPEF signals from a dilute fluorescein sample. A fiber-coupled image [as in (b)] is divided by a background-subtracted direct-PMT-detected image [as in (a)] showing a uniform 50% to 55% coupling region that extends over a diameter of ~90 $\mu$m, or 26% of the original FOV. (Color online only.)

to collect the light or the fiber was removed from the adapter and a PMT was placed in the same spot. To compare the two nondescanned images in the forward direction with an optimized detection geometry, we also include a simultaneously obtained image from the built-in, descanned, backward-collected path. As would be expected, the three images are very similar, but do display some subtle differences of import. One of the predicted advantages of proper fiber coupling is the rejection of scattered laser and ambient light because of the strict coupling conditions into the fiber. This should yield enhancements similar to those achieved by the confocal pinhole in the epidirection; however, because this is not truly confocal, epidetected descanned signals still demonstrate the highest stray light rejection. As can be seen in Fig. 2, for the forward-collected signals the fiber-coupled geometry shows considerably better background light rejection than the direct-PMT coupling. It is important to note that the direct-PMT coupling images were taken with the room lights off and with the microscope covered with a black cloth shroud, and the fiber-coupled images were taken in the presence of significant ambient room lights and with the shroud removed. With this amount of ambient light, a direct PMT image is completely saturated by background light (not shown). This configuration, therefore, cannot be used for imaging at any gain setting. This may seem a minor consideration when choosing collection geometry, but near-complete relaxation of ambient and scattered light rejection requirements results in considerably enhanced microscope usability. Thus, by using a simple multimode fiber collection geometry we are able to obtain quasi-confocal imaging with minimal free-space optical components in an economic nondescanned geometry. The ease of light shielding with a fiber-coupled scheme is of particular advantage when conducting single photon-counting detection such as TCSPC (as discussed below).

There are disadvantages to fiber-coupling laser-scanned microscope signals. Primarily, as mentioned above, deviations from proper optical geometry can lead to significant loss in both FOV and transmitted light intensity. A comparison of the images in Figs. 2(a) and 2(b) shows a perceptible narrowing in the total FOV. The coupling performance of our system is best seen, however, by taking a ratio of free-space to fiber-coupled images of a uniform sample, as shown in Fig. 2(e). This figure demonstrates that we experience a uniform 45% to 55% intensity coupling loss over a FOV of 90 $\mu$m (26% of the image), and 75% loss beyond a FOV of 200 $\mu$m in diameter. These values are only representative for our choice of fiber, condenser, and coupling aspheric lens. It is likely that further optimisation of these parameters will yield considerably improved performance beyond what we show here. Nonetheless, this FOV restriction and minor coupling loss do not prove an impediment in the typical laser-scanning microscopy performed in our laboratory, as demonstrated by our high-resolution multimodal imaging of an $\sim$60 $\mu$m-sized pollen grain, shown in Fig. 2(d).

### 3.2 *Timing Fidelity and Modal Dispersion in Multimode Fiber*

An important barrier to the wider adoption of fiber-routed signals for TCSPC was the perceived loss of timing fidelity when considering light propagation in a fiber to be governed by total internal reflection.[11] A simple analysis of the timing spread due to geometric propagation in a glass rod that guides by simple total internal reflection is given by

$$\Delta t = \frac{nl}{c}\left[\frac{1}{\sqrt{1 - NA^2/n^2}} - 1\right], \tag{1}$$

where $n$ is the glass index, $l$ is the rod length, $c$ is the speed of light in vacuum, and $NA$ is the numerical aperture of the rod.[12] For example, 2 m of multimode fiber (Thorlabs FT600EMT) with $n = 1.457$ and $NA = 0.39$ would lead to 370-ps timing uncertainty, which may be significant for many FLIM applications. This concern has been reinforced by TCSPC measurements with large fiber bundles that have shown a strong relationship between photon arrival time and the NA of the transmitted light.[12] Fiber bundles suffer from the added problem that the large bundle face and collection NA does not provide the same spatial filtering as that of a smaller fiber. Nonetheless, fiber bundles have recently begun finding a use in TCSPC-based microscopy.[14] Unlike in a glass rod, a pulse propagating in a clad fiber is mainly broadened by modal dispersion and not the simple propagation model that leads to the temporal spread predicted by Eq. (1). For multimode (and single-mode) fiber, waveguide dispersion leads to a more complicated spread in pulse dispersion, but the maximum spread in arrival times is simple to estimate[18]:

$$\Delta t_{\max} = \frac{n_{\text{core}} l}{c}\frac{\delta}{1 - \delta}, \tag{2}$$

and

$$\Delta t_{\text{rms}} \cong 0.5\Delta t_{\max}, \tag{3}$$

where $\delta$ is the difference between the index of the cladding and core and $l$ is the length of the fiber. For a 2-m length of our multimode fiber, $\delta = 0.053$, and thus we would expect *at most* 270 ps of spread. This value is similar to that found from Eq. (1), which explains why multimode fibers are often treated like simple light pipes. To get the maximum 270 ps of spread, however, would mean that we can simultaneously excite all of the modes of the fiber. In our coupling scheme, collimated light of a diameter similar to that of the core is incident onto the fiber, and we may thus expect to excite only a small subset of the allowed modes of propagation.[18] This contrasts with a simple total-internal-reflection model, which would imply that utilizing the full NA of the fiber must lead to the full spread in arrival times.

We have modified our microscope for descanned epidetected FLIM by picking off the signal just prior to incidence on the built-in PMTs and routing it to an externally mounted fast PMT connected to a commercial TCSPC timing electronics module, as described in Sec. 2.2. We also coupled the fiber to one of these detectors to test the effect of fiber collection on TCSPC timing fidelity and to provide the first demonstration of joint time-gated TCSPC FLIM/nondescanned F-CARS modalities. Because CARS is an instantaneous process compared with PMT response time, it is a good measure of the IRF of our system. Thus, by studying the timing variation and spread across the FOV on a homogenous CARS sample, we are able to ascertain the impact of using a multimode fiber on our IRF. Furthermore, by using a sample—as opposed to directly relaying laser light to the detector—we can establish an IRF image, which gives us visual insight into the effects of fiber coupling on arrival time spread. Figure 3 presents an analysis of the photon arrival times of CARS signals from a sample of pure octadecene. We parse

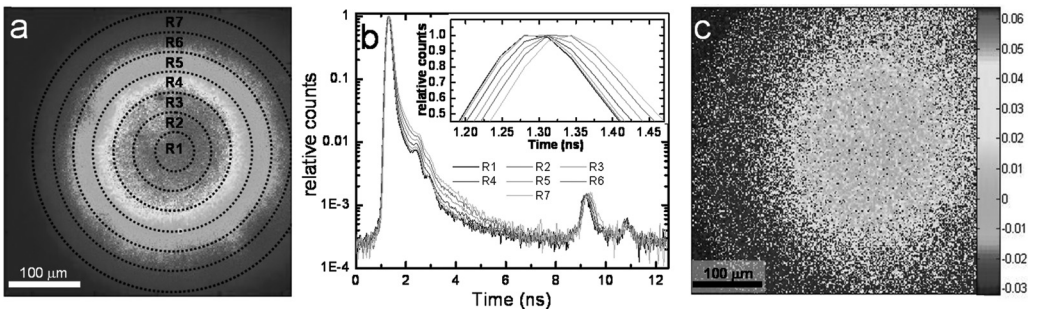


**Fig. 3** Spatial distribution of the instrument response function (IRF) in TCSPC microscopy using F-CARS (at 2880 $cm^{-1}$) in pure octadecene, collected through 2 m of multimode fiber. (a) CARS intensity profile across the entire 350 × 350 $\mu$m FOV. Color scales from blue (low) to red (high). Radial sectioning of the field for analysis of position-dependent changes in the IRF is indicated. (b) Average CARS arrival times as a function of radial position, showing that the signals are only nominally delayed as a function of off-axis displacement. Signals from the edge of the FOV arrive ∼50 ps after those in the center of the image, which is just within the timing bin resolution of our instrument (32 ps). The FWHM IRF of 200 ps shows minimal broadening due to multimodal dispersion (<17 ps). The secondary peak at 9.3 ns (20 ns after previous pulse) is from a multiple reflection through the multimode fiber. All other partially buried peaks are PMT afterpulsing artifacts. (c) A visual representation of the spread in IRF peak arrival times across the entire FOV. The color-bar units are picoseconds, and the "zero" arrival time is set at the center of the image. If necessary, this IRF map can be used to calibrate high-precision TCSPC images. (Color online only.)

the CARS image FOV into seven radial segments to explore the hypothesis that photon arrival times will increase monotonically across the FOV due the excitation of a larger proportion of higher modes in the fiber. Figure 3(b) presents the averaged CARS signal from each radial section and shows that while there is a monotonic signal delay as a function of radial position in the FOV, this delay is less than 50 ps at the edge of the image. This represents a minimal timing delay within our TCSPC timing bin resolution of 32 ps. Thus, a 2-m-long multimode fiber does not introduce significant timing variation across the 350-$\mu$m-diameter FOV considered here. In addition, as shown in the inset of Fig. 3(b), the FWHM of the IRF does not significantly broaden across the image. At the periphery of the image, a maximum shift of 46 ps and a maximum broadening of only 17 ps is observed. This timing spread is very small compared to the 270-ps spread one could expect from the excitation of the full range of allowed fiber modes. Although for most FLIM applications the time spread introduced by fiber coupling is negligible, for high-timing-resolution TCSPC applications such as determining short lifetimes, good signal-to-noise measurements of the IRF are important. Typically, the IRF is treated as a constant across the image, and it is collected as a global parameter to be deconvolved from the position-dependant TCSPC image. In our case, one could construct an IRF map for pixel-by-pixel deconvolution. The FLIM signal can then be extracted directly by calibrating against such an IRF map. For example, a CARS arrival time map taken from pixel-by-pixel analysis of the arrival histogram is presented in Fig. 3(c), and similar analysis could be useful when using a more dispersive fiber. The radial symmetry of the IRF map further allows averaging of pixels within ring segments to provide improved signal-to-noise in an IRF map.

As demonstrated by Ly et al., the fact that CARS is indistinguishable from the IRF in a TCSPC experiment allows for cocollection and subsequent time-gated separation of CARS and FLIM on a single detector.[9] We demonstrate this modality on a pure F-CARS signal coupled through a fiber while simultaneously performing FLIM. Figure 4 presents separation of CARS signals in oil from a TPEF background of fluorescein in aqueous solution. The signal from the oil droplets arrives within the IRF time, whereas those from the aqueous solution arrive with an exponential decay time of 3.4 ns, as shown in Fig. 4(a). Figure 4(b) shows an image of all photons arriving over a 300-ps timescale about the IRF peak (at 1.22 ns) and represents the CARS image. Figure 4(c) shows an image of all photons arriving 300 ps after this time (1.55 to 12.5 ns) and represents the TPEF image. In addition, a region in the FOV that could look like an oil drop in the FLIM image is absent from the CARS image and is identified as an air bubble.

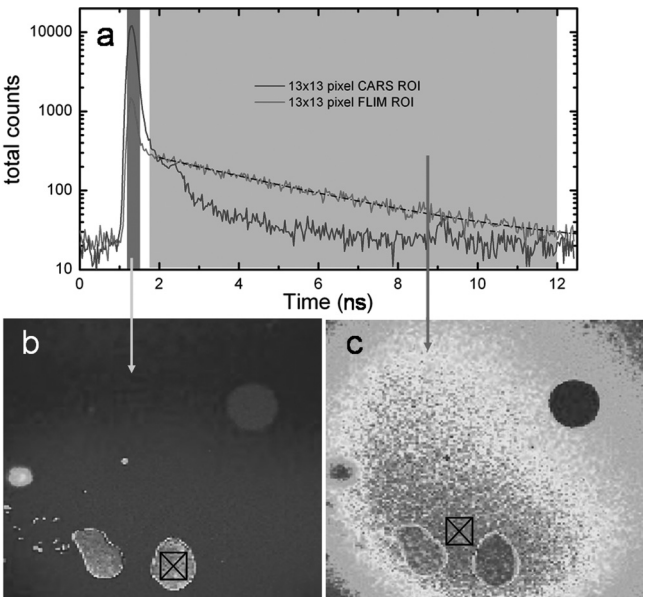


**Fig. 4** Time-gated F-CARS and FLIM imaging on a single detector. The sample is comprised of oil droplets in an aqueous fluorescein solution. (a) TCSPC timing histogram of the two 13×13 pixel regions of interest marked in (b) and (c). The two time gates are shown as gray regions. (b) Image of all photons arriving in the vicinity of the IRF peak, representing CARS signals from the oil. (c) Image of all photons arriving between 500 ps after the IRF peak and the end of the laser repetition period, representing TPEF signal from fluorescein. A FLIM analysis in (a) yields a relaxation lifetime of 3.4 ± 0.3 ns for fluorescein. The blue circle in the upper right corner of both images is identified as an air bubble. For (b) and (c) color scales from blue (low) to red (high) with the figures independently scaled for contrast. (Color online only.)

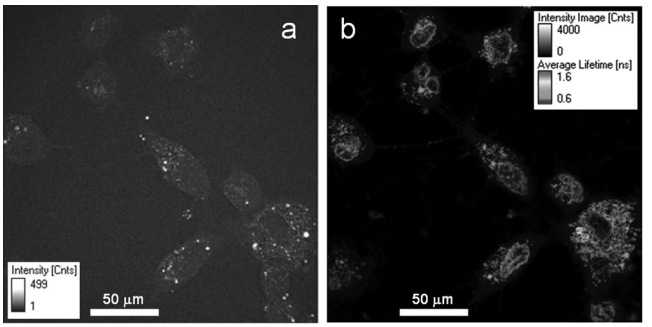


**Fig. 5** Simultaneous multichannel CARS + FLIM imaging of live HuH-7 cells. (a) F-CARS image collected through a multimode fiber. (b) Epicollected FLIM images showing spatial segregation of the Hoechst and DiO stains. The average Hoechst lifetime in the nucleus is 1.6 ± 0.4 ns and that of the DiO in the cytoplasm is sub 1 ns. In the CARS channel, a 650 ± 30 nm bandpass filter is placed between the condenser and the fiber. (Color online only.)

As a first step toward conducting future FRET + CARS experiments, we demonstrate concurrent two-channel TCSPC-based FLIM and CARS imaging of live cells stained with Hoechst3342 (Hoechst) and DiOc6(3) (DiO). One of the channels is epidetected FLIM and the other is simultaneous fiber-coupled F-CARS imaging onto a standard PMT. Hoechst is a nucleus-staining dye, and DiO typically stains the ER in the cytoplasm. HuH-7 cells are selected for their high lipid droplet content, which is imaged by CARS. Figure 5 shows the resulting CARS and FLIM images. Strong CARS signals are seen from lipid droplets in the cytoplasm. A lifetime map reveals the Hoechst in the nucleus to have an average fluorescence decay lifetime of 1.6 ± 0.4 ns and that of DiO in the cytoplasm to be <1 ns. Interestingly, we have found that DiO displays a wide range of lifetimes in the cytoplasm, ranging from 0.4 to 1.0 ns depending on its binding locale. To the best of our knowledge, this is the first estimate of the decay lifetime of intracellular DiO dye. The nuclear-bound Hoechst lifetime reported here is in good agreement with values in the literature.[19,20]

## 4 Conclusion

We have presented the novel combination of FLIM and true forward-collected CARS microscopy. We also presented single-detector F-CARS + FLIM imaging using time-gated TCSPC analysis. To accomplish this, we developed a small adapter for an inverted laser-scanning microscope that fits on the condenser and couples light into a standard multimode fiber for routing to off-board detectors. We demonstrated the advantages of fiber-coupling laser-scanning microscope signals: significant reduction in the need to regulate stray light; improved flexibility in microscope design and detector placement; and the ease of collecting nondescanned light for high-time-resolution TCSPC applications. We outlined key considerations for choosing a proper fiber-coupling geometry in a laser-scanning microscope and provided suggestions for how to do this. We have furthermore aimed to show, in detail, the minor effects that fiber dispersion has on TCSPC timing, as well as a way to calibrate high-timing-resolution measurements for those effects that may be present. We have found that with a 2-m-long 0.60-mm-diameter-core 0.39-NA multimode fiber we get no more than 50 ps of pulse delay spread across a 350-$\mu$m-diameter image (the instrument response function of our setup is 200 ps). We determined that broadening of the IRF is considerably less than the pulse delay spread, indicating that light from a given location in the sample only excites a narrow and well-defined subset of fiber modes. Although we highlight the use of fiber coupling for forward-detected light—mostly because of our interest in CARS, which is mainly forward propagating, and because commercial confocal inverted microscopes are well equipped for epidetection—fiber coupling of nondescanned epicollected light poses no additional difficulties. Drawbacks to coupling though multimode fiber are a modest reduction in the field of view and coupling losses in transmission. With our unoptimised coupling geometry, we are able to achieve >50% transmission in the center of the image and a flat-intensity field of view over 25% (90-$\mu$m diameter) of the image. Imaging beyond this FOV suffers from gradual apodization of light but remains spatially undistorted. We suggest that the drawbacks of using a multimode fiber can be further mitigated with the use of a larger-core graded-index fiber, which is expected to display even lower modal dispersion.

### Acknowledgments

This research was largely funded by a joint NRC-NSC-ITRI Canada-Taiwan Cooperation project "Digital FLIM-CARS Microscopy." We would like to thank Rodney Lyn for his expertise and time in HuH-7 cell sample preparation and general discussion. We gratefully acknowledge Guillaume Labroille for fruitful discussions and for his input into optical alignment and layout design.

### References

1. W. Becker, A. Bergmann, M. A. Hink, K. Konig, K. Benndorf, and C. Biskup, "Fluorescence lifetime imaging by time-correlated single-photon counting," *Microsc. Res. Tech.* **63**, 58–66 (2004).
2. K. Suhling, P. M. W. French, and D. Phillips, "Time-resolved fluorescence microscopy," *Photochem. Photobiol. Sci.* **4**, 13–22 (2005).
3. P. R. Selvin, "The renaissance of fluorescence resonance energy transfer," *Nat. Struct. Biol.* **7**, 730–734 (2000).
4. P. O. Provenzano, K. W. Eliceiri, J. M. Campbell, D. R. Inman, J. G. White, and P. J. Keely, "Collagen reorganization at the tumor-stromal interface facilitates local invasion," *BMC Med.* **4**, 38 (2006).
5. E. O. Potma and X. S. Xie, "Detection of single lipid bilayers with coherent anti-Stokes Raman scattering (CARS) microscopy," *J. Raman. Spectrosc.* **34**, 642–650 (2003).
6. J.-X. Cheng, A. Volkmer, and X. S. Xie, "Theoretical and experimental characterization of coherent anti-Stokes Raman scattering microscopy," *J. Opt. Soc. Am. B* **19**, 1363–1375 (2002).
7. J.-X. Cheng, A. Volkmer, L. D. Book, and X. S. Xie, "An epi-detected coherent anti-Stokes Raman scattering (E-CARS) microscope with high spectral resolution and high sensitivity," *J. Phys. Chem. B* **105**, 1277–1280 (2001).
8. I. W. Schie, T. Weeks, G. P. McNerney, S. Fore, J. K. Sampson, S. Wachsmann-Hogiu, J. C. Rutledge, and T. Huser, "Simultaneous forward and epi-CARS microscopy with a single detector by time-correlated single photon counting," *Opt. Express* **16**, 2168–2175 (2008).
9. S. Ly, G. McNerney, S. Fore, J. Chan, and T. Huser, "Time-gated single photon counting enables separation of CARS microscopy data from multiphoton-excited tissue autofluorescence," *Opt. Express* **15**, 16839–16851 (2007).
10. S. O. Konorov, C. H. Glover, J. M. Piret, J. Bryan, H. G. Schulze, M. W. Blades, and R. F. B. Turner, "In situ analysis of living embryonic stem cells by coherent anti-Stokes Raman microscopy," *Anal. Chem.* **79**, 7221–7225 (2007).

11. W. Becker, *Advanced Time-correlated Single-photon Counting Techniques*, pp. 282–284, Springer, Heidelberg (2005).
12. A. Liebert, H. Wabnitz, D. Grosenick, and R. Macdonald, "Fiber dispersion in time domain measurements compromising the accuracy of determination of optical properties of strongly scattering media," *J. Biomed. Opt.* **8**, 512–516 (2003).
13. M. Kress, T. Meier, R. Steiner, F. Dolp, R. Erdmann, U. Ortmann, and A. Rück, "Time-resolved microspectrofluorometry and fluorescence lifetime imaging of photosensitizers using picosecond pulsed diode lasers in laser scanning microscopes," *J. Biomed. Opt.* **8**, 26–32 (2003).
14. W. Becker, A. Bergmann, and C. Biskup, "Multi-spectral fluorescence lifetime imaging by TCSPC," *Microsc. Res. Tech.* **70**, 403–409 (2007).
15. A. F. Pegoraro, A. Ridsdale, D. J. Moffatt, Y. Jia, J. P. Pezacki, and A. Stolow, "Optimally chirped multimodal CARS microscopy based on a single ti:sapphireoscillator," *Opt. Express* **17**, 2984–2996 (2009).
16. A. D. Slepkov, A. Ridsdale, A. F. Pegoraro, G. Labroille, and A. Stolow, "Optimizing spectral resolution in supercontinuum-generation-based multimodal fs CARS microscopy," *CLEO 2010 Technical Digest*, CWD2, 1–2 (2010).
17. R. K. Lyn, D. C. Kennedy, S. M. Sagan, D. R. Blais, Y. Rouleau, A. F. Pegoraro, X. S. Xie, A. Stolow, and J. P. Pezacki, "Direct imaging of the disruption of hepatitis C virus replication complexes by inhibitors of lipid metabolism," *Virology* **394**, 130–142 (2009).
18. B. E. A. Saleh and M. C. Teich, *Fundamentals of Photonics*, Chap. 8, Wiley, New York (1991).
19. ISS, Inc., "Lifetime data of selected fluorophores," ⟨http://www.iss.com/resources/fluorophores.html⟩, accessed May 15, 2010.
20. S. Murata, P. Herman, H.-J. Lin, and J. Lakowicz, "Fluorescence lifetime imaging of nuclear DNA; effect of fluorescence resonance energy transfer," *Cytometry* **41**, 178–185 (2000).